Supporting Information

Defect-Tailored ZnO Nanoflowers Enable Efficient, Metal-Free Ammonia Synthesis through Coupled Piezoelectric and Photocatalytic Activation

Authors: Jyh-Xuan Wang[a‡], Hsun-Yen Lin[a‡], Kuang Yuan Tu, and Jyh-Ming Wu[a, b*]

[a] Department of Materials Science and Engineering, National Tsing Hua University

101, Section 2 Kuang Fu Road, Hsinchu 300, Taiwan.

[b] High Entropy Materials Center, National Tsing Hua University

101, Section 2 Kuang Fu Road, Hsinchu 300, Taiwan.

*Corresponding author: Prof. J. M. Wu, Email: wujm@mx.nthu.edu.tw

[‡]:Authors equal contribution

*Corresponding author: Prof. J. M. Wu, Email: wujm@mx.nthu.edu.tw

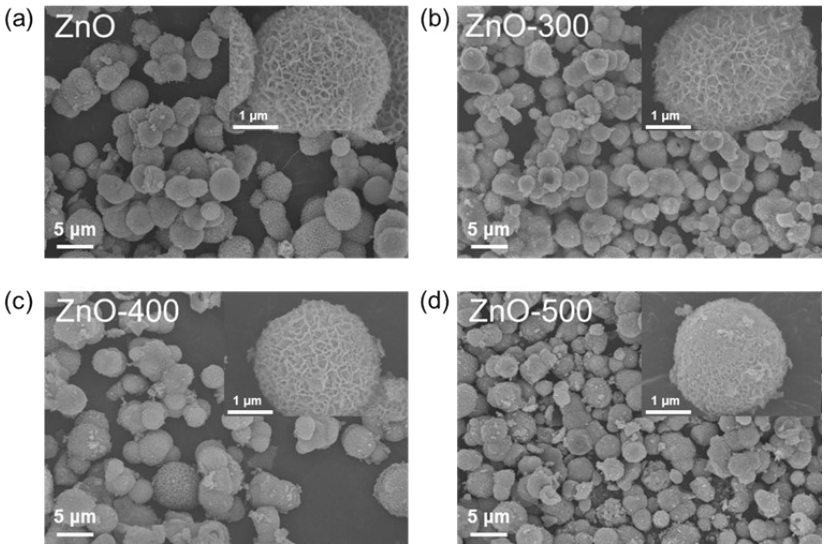

Figure S1. SEM images of (a) pristine ZnO, (b) ZnO-300, (c) ZnO-400, and (d) ZnO-500 with the high-magnification image insets.

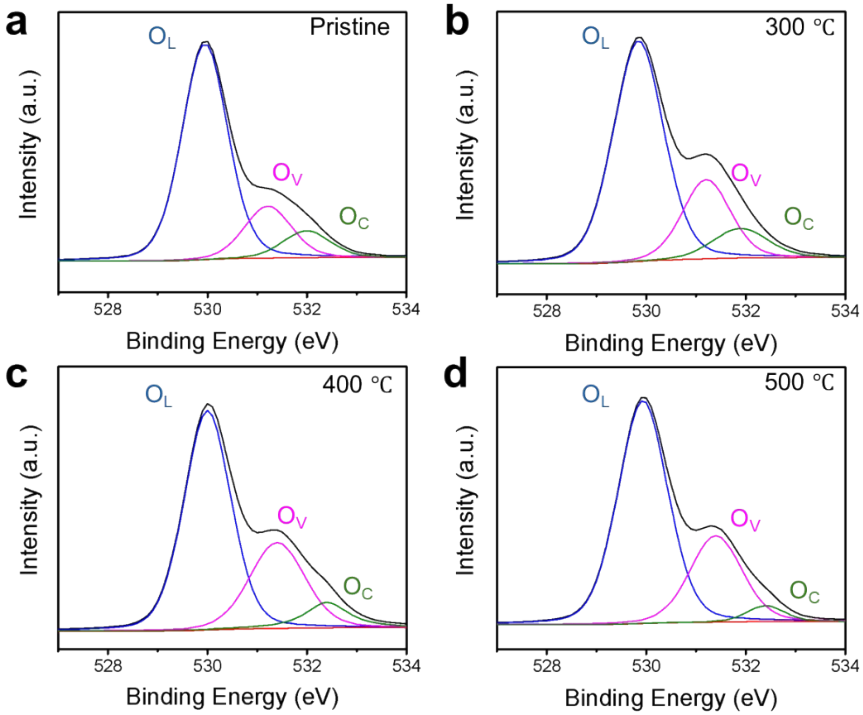

Figure S2. XPS O 1s spectra of (a) pristine ZnO, (b) ZnO-300, (c) ZnO-400, and (d) ZnO-500.

Supporting Information of S1

A gradual narrowing of the band gap is observed with increasing annealing

temperature. This redshift can be attributed to the increasing concentration of oxygen vacancies, which introduce localized defect states near the conduction band edge. These defect states effectively reduce the band gap, enhancing visible-light absorption and improving photocatalytic activity under solar irradiation. The band gap in ZnO-500 is 3.18 eV, which correlates with its highest oxygen vacancy concentration, as also supported by EPR and XPS results.

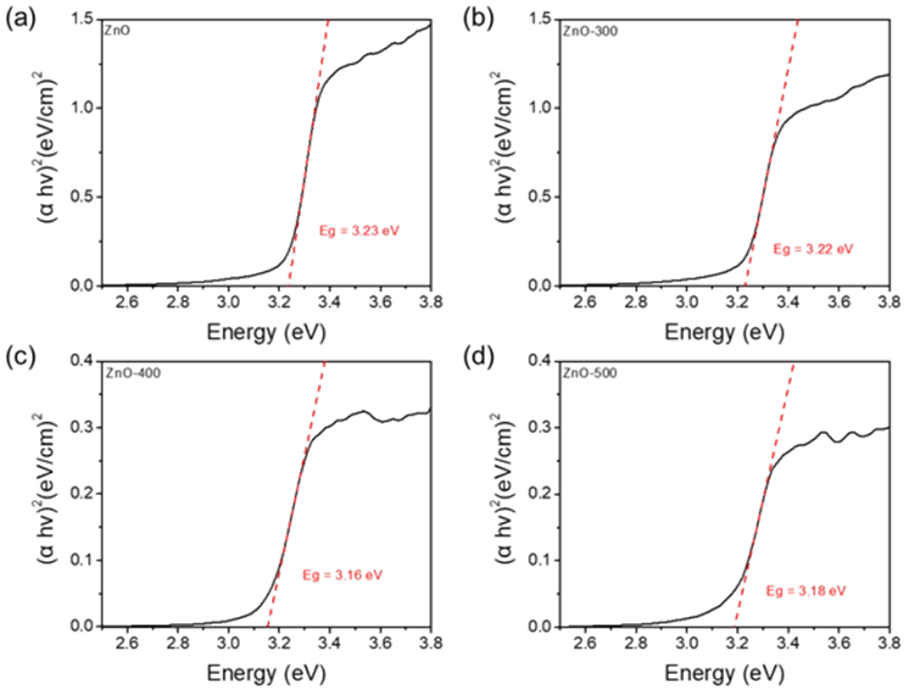

Figure S3. presents the UV–vis diffuse reflectance spectroscopy (UV-DRS) results and corresponding Tauc plots of (a) pristine ZnO, (b) ZnO-300, (c) ZnO-400, and (d) ZnO-500, used to estimate the optical band gap energies of each sample.

Supporting Information of S2

Figure S4 shows the X-ray photoelectron spectroscopy valence band maximum (XPS-VBM) spectra of ZnO samples annealed at different temperatures. The VBM values were estimated by extrapolating the linear portion of the leading edge of each spectrum to the baseline. The valence band maximum values, determined from the extrapolation of the leading edge of the XPS spectra, are 2.67 eV for pristine ZnO and

ZnO-300, 2.61 eV for ZnO-400, and 2.52 eV for ZnO-500. These results indicate a progressive downward shift of the VBM with increasing annealing temperature, especially evident in ZnO-400 and ZnO-500. This shift can be attributed to the formation of oxygen vacancies, which modify the electronic structure by introducing mid-gap states and lowering the effective VBM position. The reduced VBM suggests enhanced band bending and stronger internal electric fields, which are favorable for improved charge separation and surface redox activity during the photocatalytic and piezocatalytic nitrogen reduction reaction (NRR).

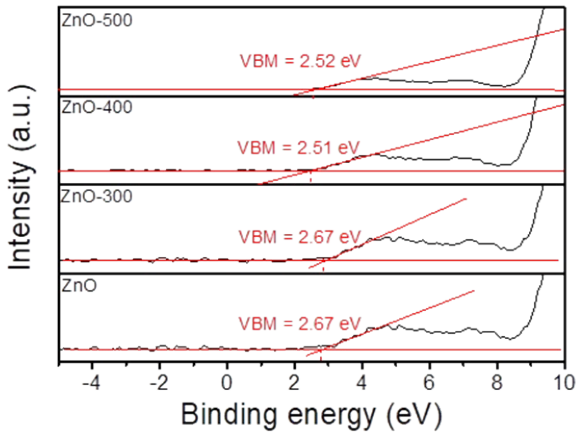

Figure S4. XPS-VBM results of ZnO under different annealing temperatures indicating the valence band maximum of each sample.

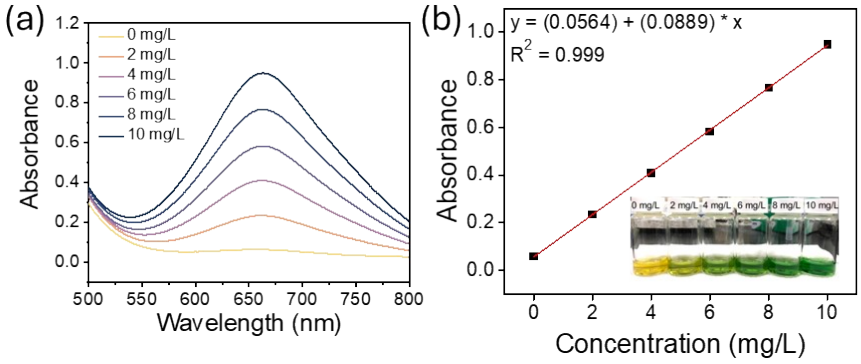

Figure S5. Calibration curve of the indophenol blue method (a) UV-vis spectra and (b) the calibration curve of absorbance and ammonia concentration.

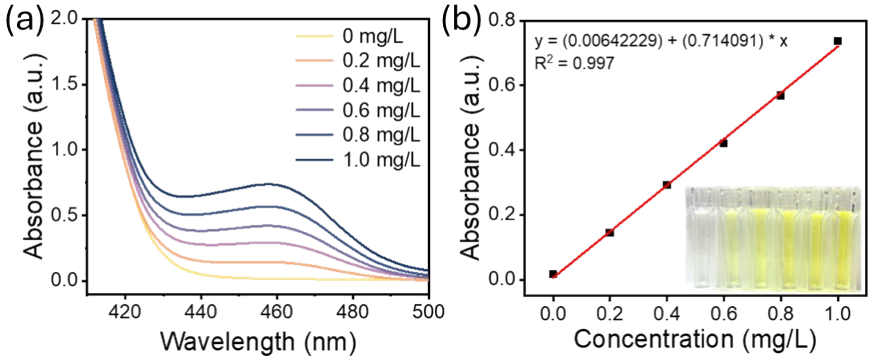

Figure S6. Calibration curve of the Watt and Chrisp method (a) UV-vis spectra and (b) the calibration curve of absorbance and N_2H_4 concentration.

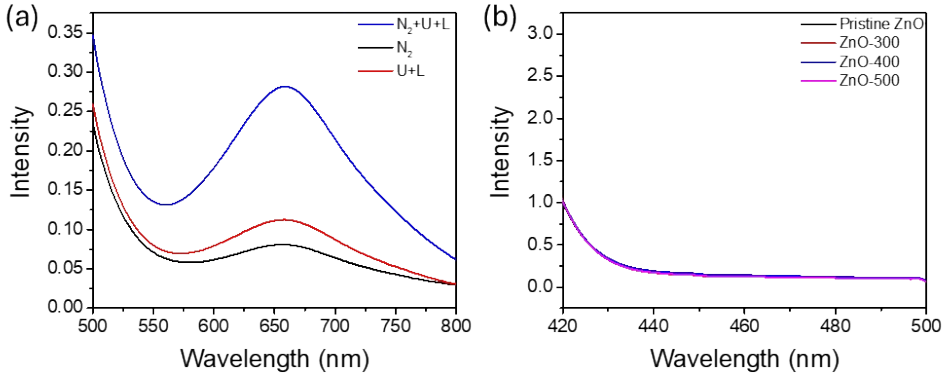

Figure S7. (a) UV-vis spectra of ZnO-300 under different catalytic conditions. U: ultrasonication, L: light irradiation, and N_2: N_2 pumping. (b) UV-vis spectra for Watt and Chrisp method of the ZnO NFs under different annealing temperatures.

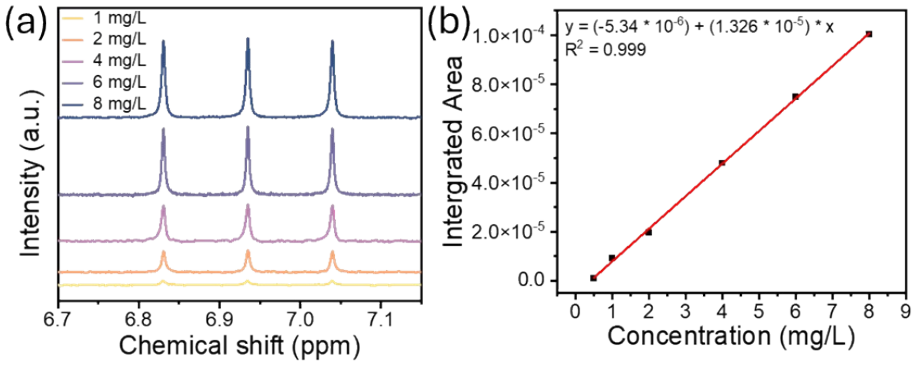

Figure S8. Calibration curve of the NMR quantification method (a) NMR spectra and (b) the calibration curve of NMR integrated area and ammonia concentration.

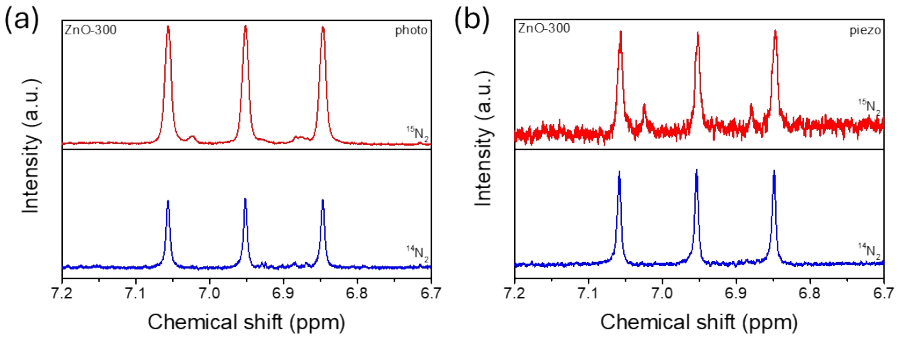

Figure S9. NMR spectra of $^{15}NH_4^+$ and $^{14}NH_4^+$ detection of ZnO-300 through (a) photocatalytic process and (b) piezocatalytic process.

Table S1. Comparison table of NH_3 production rates using different catalytic sources and catalysts.

Catalytic source	**Catalyst**	**NH_3 production rate**	**Reference**
Piezo/Photo	ZnO-O_V	1765.3 μg g_{cat}^{-1} h^{-1}	This work
Photo	Fe-TiO_2	1091.4 μg g_{cat}^{-1} h^{-1}	[1]
Photo	Fe-Bi_2MoO_6	1810.5 μg g_{cat}^{-1} h^{-1}	[2]
Photo	g-C_3N_4-C_V	1428 μg g_{cat}^{-1} h^{-1}	[3]
Piezo	Ag/ZnO	66.64 μg g_{cat}^{-1} h^{-1}	[4]
Piezo	Ag/Bi_5O_7I	1111.8 μg g_{cat}^{-1} h^{-1}	[5]
Piezo/Photo	$BaTiO_3$-O_V	1813.9 μg g_{cat}^{-1} h^{-1}	[6]

Supporting Information of S3

Calculation details

Initially, the unit cell of ZnO was relaxed using a 10 × 10 × 6 gamma-centered k-point mesh. Subsequently, to explore the surface properties of the ZnO (100) surfaces, a 2 × 2 supercell with a ZnO (100) surface was constructed. Then the oxygen vacancy

defect was introduced on the surface. The final model can be divided into pristine ZnO and ZnO-O_V for further computation, as shown in Figure S10. To maintain a similar k-point density in the supercell as in the unit cell, the k-point mesh was adjusted to a 5 × 3 × 1 gamma-centered mesh. The surface model comprised six layers, with the lower three layers constrained to their bulk configuration throughout all calculations. Additionally, a vacuum layer with a width of 20 Å was included to prevent interactions between periodic images. The adsorption energy E_{ads} of N_2 on the surface of ZnO was calculated through the following equation:

$$E_{ads} = E_{total} - E_{surface} - E_{N_2}$$

where E_{total}, E_{N_2}, and $E_{surface}$ are the total energies of the adsorbed system, isolated nitrogen molecules, and pristine surface, respectively.

In order to compute partial atomic charges for all systems, we performed charge analysis calculations to determine the Bader charge and charge density difference (CDD) for ZnO. The CDD can be obtained by following the equation:

$$CDD = Charge\ density_{total\ system} - Charge\ density_{surface} - Isolated_{N_2}$$

Density of state analysis has also been conducted to investigate the energy band structure of ZnO and ZnO-O_V and the defect state formation. The model of ZnO-O_V with different percent biaxial strain has also been made in order to simulate the applied stress on the piezoelectric ZnO surface.

The reaction free energy was calculated by following the equation:

$$E_{free} = E_{total} - E_{surface} - n\mu_N - m\mu_H$$

where E_{total} and $E_{surface}$ are the total energies of the adsorbed system and bare surface, respectively. And μ_N and μ_H are the chemical potentials of the nitrogen atom and hydrogen atom, respectively*[7]*.

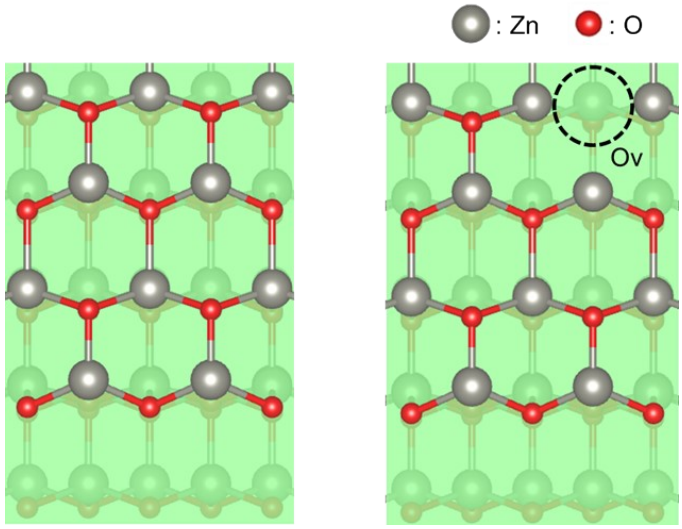

Figure S10. DFT calculation model of pristine ZnO (100) slab (left) and ZnO (100) slab with oxygen vacancy (right).

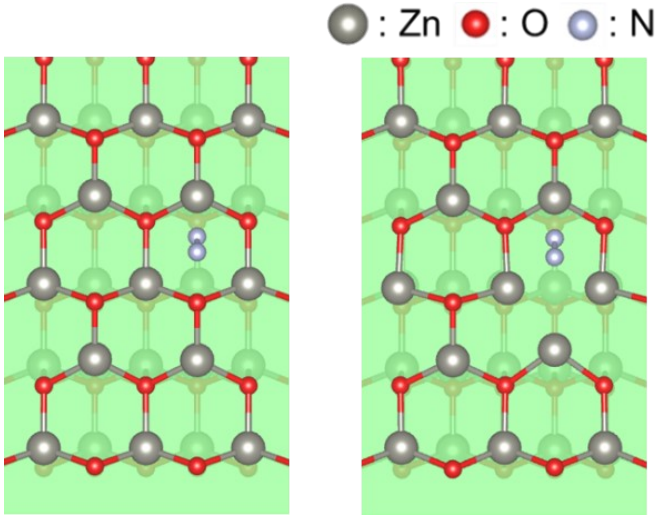

Figure S11. DFT model of pristine ZnO (left) and ZnO-O_V (right) after the adsorption of nitrogen by end-on mode at the hollow sites.

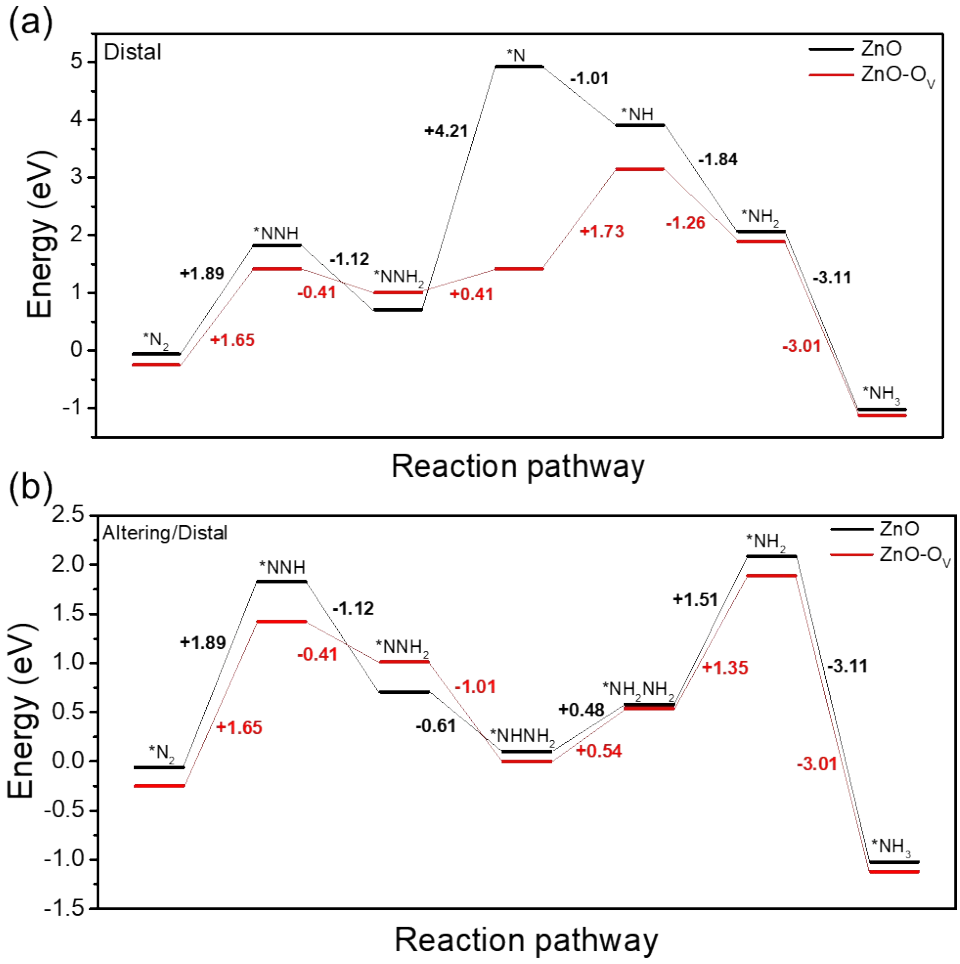

Figure S12. NRR free energy diagram of ZnO and ZnO-O_V through (a) associative distal pathway and (b) mix pathway. The calculation results indicate that the energy barrier of the distal pathway is larger, thus it is not energy-favorable in our system.

Supporting Information of S4

Hydrogenation sequences of associative altering pathway, indicating the transition from $^*N_2$ to $^*NH_3$.

$$*N_2 \xrightarrow{H^+ + e^-} *NNH$$

$$*NNH \xrightarrow{H^+ + e^-} *NHNH$$

$$*NHNH \xrightarrow{H^+ + e^-} *NHNH_2$$

$$*NHNH_2 \xrightarrow{H^+ + e^-} *NH_2NH_2$$

$$*NH_2NH_2 \xrightarrow{H^+ + e^-} *NH_2 + NH_3$$

$$*NH_2 \xrightarrow{H^+ + e^-} *NH_3$$

Table S2. Composition of the indophenol blue indicator.

Solution	**Composition**
A	4.97 g salicylic acid + 4.39 g sodium citrate in 100 ml, 0.625 M KOH solution
B	$C_5FeN_6Na_2O$ solution (10 mg/ml)
C	4% NaClO solution

References

[1] Y. Bo, H. Wang, Y. Lin, T. Yang, R. Ye, Y. Li, C. Hu, P. Du, Y. Hu, Z. Liu, R. Long, C. Gao, B. Ye, L. Song, X. Wu, Y. Xiong, Altering Hydrogenation Pathways in Photocatalytic Nitrogen Fixation by Tuning Local Electronic Structure of Oxygen Vacancy with Dopant, Angewandte Chemie International Edition, 60 (2021) 16085-16092.

[2] Q. Meng, C. Lv, J. Sun, W. Hong, W. Xing, L. Qiang, G. Chen, X. Jin, High-efficiency Fe-Mediated Bi2MoO6 nitrogen-fixing photocatalyst: Reduced surface work function and ameliorated surface reaction, Applied Catalysis B: Environmental, 256 (2019) 117781.

[3] Y. Zhang, J. Di, P. Ding, J. Zhao, K. Gu, X. Chen, C. Yan, S. Yin, J. Xia, H. Li, Ultrathin g-C3N4 with enriched surface carbon vacancies enables highly efficient photocatalytic nitrogen fixation, Journal of Colloid and Interface Science, 553 (2019) 530-539.

[4] F. Peng, J. Lin, H. Li, Z. Liu, Q. Su, Z. Wu, Y. Xiao, H. Yu, M. Zhang, C. Wu, W. Wang, C. Lu, Design of piezoelectric ZnO based catalysts for ammonia production from N2 and H2O under ultrasound sonication, Nano Energy, 95 (2022) 107020.

[5] L. Chen, W. Zhang, J. Wang, X. Li, Y. Li, X. Hu, L. Zhao, Y. Wu, Y. He, High piezo/photocatalytic efficiency of Ag/Bi5O7I nanocomposite using mechanical and solar energy for N2 fixation and methyl orange degradation, Green Energy & Environment, 8 (2023) 283-295.

[6] J. Yuan, W. Feng, Y. Zhang, J. Xiao, X. Zhang, Y. Wu, W. Ni, H. Huang, W. Dai, Unraveling Synergistic Effect of Defects and Piezoelectric Field in Breakthrough Piezo-Photocatalytic N2 Reduction, Advanced Materials, 36 (2024) 2303845.

[7] L. Tian, Y.-S. Liao, J.-P. Chou, Z. Tan, J.L. Chen, J.-H. Lee, T.W. Benedict Lo, Y.-K. Peng, Facet-dependent peroxo species regulate product distribution and H2O2 utilization in CeO2-catalyzed aniline oxidation, Journal of Materials Chemistry A, 11 (2023) 14034-14042.